Proceedings of the Design Society, Volume 5: ICED25
https://doi.org/10.1017/pds.2025.10136

Design of a Reconfigurable Crawler based on Waterbomb Origami

Lingchen Kong and Yaoyao Fiona Zhao✉

McGill University, Montreal, Quebec, Canada

✉ yaoyao.zhao@mcgill.ca

ABSTRACT: Inspired by nature, where organisms adapt their shapes to navigate complex challenges, engineering systems can benefit from reconfigurable designs that move beyond rigid, conventional strategies. Reconfiguration offers a promising solution for systems to adapt dynamically to changing operational requirements. Origami, known for its ability to transform from simple 2D sheets into intricate 3D structures, provides a powerful framework for designing adaptable and reconfigurable systems. In this study, a waterbomb origami-based (WOB) crawler is proposed featuring reverse movement without changing actuation. The unfolding and folding process of the WOB enables motion due to the friction between the vertex and the ground, whereas the reverse movement is achieved by leveraging the local bistability of one WOB crease.

KEYWORDS: Reconfiguration, Waterbomb origami, Robotics

1. Introduction

The function of a system is often directly encoded in its shape, structure and arrangement of the parts, regarded as the configuration (Haupt et al., 2013; Mintchev et al., 2016). When the desired operating characteristics of the system change, conventional systems based on traditional design strategies, which are designed for a single task fail to be adaptive. In this case, reconfiguration provides a promising solution that can generate different configurations to meet the new specifications. In nature, the unknown environment and the need for survival determine the locomotion strategies of animals, including moving modals, gaits and dexterity, energy balance and saving, control strategies, etc. (Lock et al., 2013). For example, birds can switch the flying modes by unfolding or retracting the wings to increase the lift or keep the high speed (Mintchev et al., 2016) and amphibious animals lower the drag by streaming their morphology during swimming while maintaining their mobility on land (Baines et al., 2019). Inspired by biological organisms in nature, reconfigurable systems that can adapt themselves for different tasks gain a lot of attention in engineering applications, including aerospace (Li et al., 2018; Hassan et al., 2008), metamaterials (Wu et al., 2022; Bordiga et al., 2024), robotics (Patel et al., 2023; Chen et al., 2022) and bio-medical devices (Gu et al., 2023; Kuribayashi et al., 2006), etc.

However, the real potential of reconfiguration in engineering is often bounded by traditional design strategies and rigid materials (Mintchev et al., 2016). In this case, shape-changing structures can provide new insights for unleashing the true potential of reconfiguration. In the context of shape-reconfiguration, shape-changing structures, which can alter their form and geometry in response to external stimuli and user input, align seamlessly with the concept of shape-reconfiguration. In the realm of mobile robotics, the ability of shape-changing can be emphasized in two aspects: generating motion and achieving multifunctionality. Generating motion is essential as it enables robots to navigate complex and dynamic environments. Multi-functionality allows robots to adapt to diverse tasks by altering their shape and mechanical properties, making them more versatile and cost-effective. Research in this field has focused on developing robots with high moving efficiency (Mao et al., 2022;

Tang et al., 2020; Wang et al., 2023, 2024). Among these, origami-based designs stand out for their ability to morph from two-dimensional sheets into complex three-dimensional shapes. However, many efforts have been made focusing on generating motion for mobile robots (Ze et al., 2022; Pagano et al., 2017; Ze et al., 2022) while limited works focus on utilizing the reconfiguration of origami to achieve multi-functionality.

In this work, a locomotion robot is proposed based on the waterbomb-origami-base (WOB). As a classic type of origami, waterbomb origami can be categorized into different variants, such as 6-crease waterbomb and 8-crease waterbomb, depending on the number of creases radiating from the center vertex. A key feature of waterbomb origami is the inherent bistability, allowing it to maintain distinct configurations without continuous external input. Leveraging this property, the WOB-based robot achieves multi-modal locomotion, including bidirectional motion, without altering the actuation mechanism. In each stable configuration, one vertex of the WOB contacts the ground, generating specific anisotropic friction. By transitioning between these configurations, the robot modulates the anisotropic friction against the ground, enabling reversible motion.

The remainder of this paper is organized as follows: Section 2 presents the design of the WOB crawler, detailing its geometry, kinematic analysis, the locomotion mechanism enabled by reconfiguration and anisotropic friction and the fabrication process. The results of the kinematic analysis are first discussed in Section 3, followed by the experiment setup. Then theoretical predictions are compared with experimental findings. Finally, Section 4 concludes the paper, summarizing key insights and proposing directions for future research.

2. Design of WOB crawler

This section introduces the design of theWOB crawler. The design integrates geometric variables such as the origami structure and track patterns with a bistability-based reconfiguration mechanism, enabling the WOB to switch between two configurations. Each configuration features a distinct vertex and anisotropic friction profile, which are critical for achieving reverse motion. The kinematic analysis describes the deformation behavior of theWOB in each configuration and calculates the trajectories of vertices, which can provide certain insight to inform the design of the crawler.

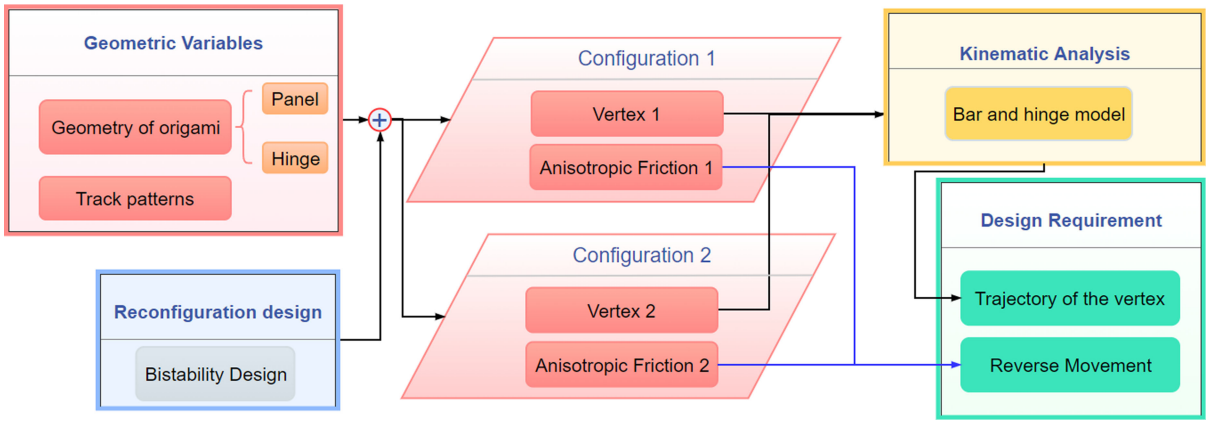

Figure 1. Design process of WOB crawler

2.1. WOB geometry description

The crease pattern for a WOB is shown in Fig.2(A), where the mountain fold and valley fold are represented by solid lines and dashed lines respectively (mountain fold and valley fold have different lengths, represented by OA_i and OB_i). Each WOB has eight identical panels, four external feet (the outer end of mountain folds, represented by $A_1 - A_7$ in Fig.2(A)) and four internal feet (the outer end of valley folds, represented by $B_1 - B_7$ in Fig.2(A)). The fold lines are arranged such that adjacent lines are

separated by 45°. Under fully symmetric conditions, all the mountain (valley) folds have the same angle θ_m (θ_v), which is the angle between the mountain (valley) fold and the vertical axis (V), as shown in Fig.2(B) and (C). Globally,WOB exhibits two distinct stable equilibrium positions, as shown in Fig.2(B) and (C). Locally, each valley fold of folded WOB in position 1 can be individually inverted to the mountain fold without influencing other creases.

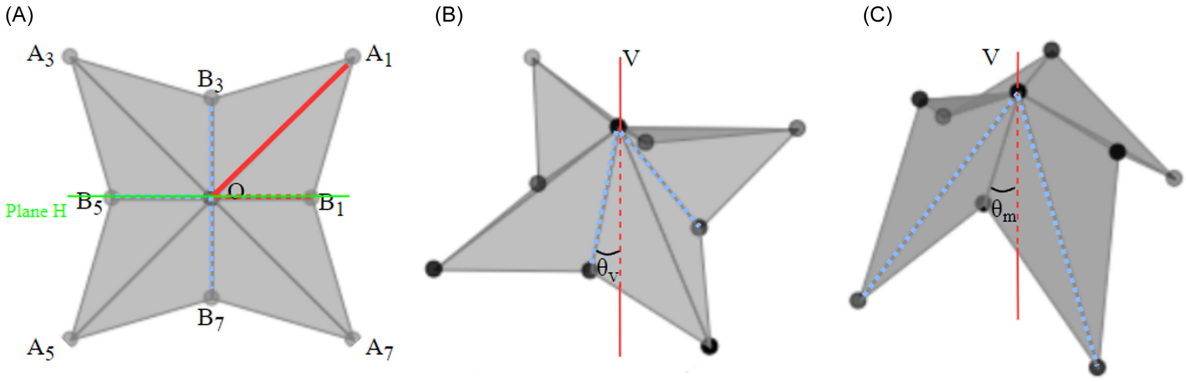

Figure 2. Diagram of the WOB. A) WOB geometry description. B) WOB in global equilibrium Position 1. C) WOB in global equilibrium Position 2

2.2. Kinematic analysis of WOB

In order to use WOB to generate motion, kinematic analysis is required to describe the deformation and unfolding/folding behaviors of WOB. Notably, in kinematic analysis, rigid body assumption is applied, i.e. the deformation at hinges is exclusively considered without any in-plane deformation of panels, and the origami is rigid folding. There are two main computational techniques to model origami behaviors: Angle-/plate-based and Vertex-/truss-based models (Zhou et al., 2023). In the Angle-/plate-based models, variables are commonly chosen as the fold angles of each fold line, which are used to form the constraining equations based on the trigonometry to solve the folding trajectory (Zhu et al., 2022). However, in more complex scenarios, additional degrees of freedom (DoFs) require more boundary conditions to describe the deformation of WOB, which limits the performance of Angle-/plate-based models. In this case, Vertex-/truss-based models, also known as the bar and hinge models, focus on the displacement field of each vertex and provide a general solution.

Based on the pin-jointed framework in structural mechanics, the statical and kinematic determinacy of the pin-jointed framework can be determined by Maxwell's rule, which involves the relationship between the number of joints, bars and constraints (Pellegrino and Calladine, 1986). By simplifying each origami panel into the interconnection of bars and joints, three fundamental elastic behaviors of origami can be modeled: in-plane stretching and shear, out-of-plane bending of panels and folding along creases (Filipov et al., 2017). This work specifically focuses on analyzing the folding and unfolding behavior along the creases.

It is worth mentioning that the folding of the panels is replaced by the rotation of two neighboring panels along the bending hinge, where a spring with rotational stiffness is assigned (Fig.3). The governing equations of pin-jointed frameworks build the relationship among nodal force **(f)**, bar tension **(t)**, nodal displacement **(d)** and bar elongation **(e)**, using three metrics: equilibrium matrix **(A)**, compatibility matrix (kinematic matrix) **(C)** and a diagonal matrix **(G)** involving axial bar stiffness parameters (Eq.1).

$$\mathbf{At} = \mathbf{f}, \quad \mathbf{Cd} = \mathbf{e}, \quad \mathbf{Ge} = \mathbf{t}. \tag{1}$$

The equilibrium matrix and compatibility matrix are highly related to the number and arrangement of bars and joints, which cover the connection information between each bar and joint. For the detailed calculation of the equilibrium matrix, readers can refer to the work of Pellegrino et al. (Pellegrino and Calladine, 1986).

One advantage of the bar and hinge model is that it can both deal with kinematic and mechanics analysis, by analyzing compatibility matrix and stiffness matrix, respectively. In the kinematic analysis, the focus will fall on the vector subspaces of the equilibrium matrix and compatibility matrix, where the nullspace

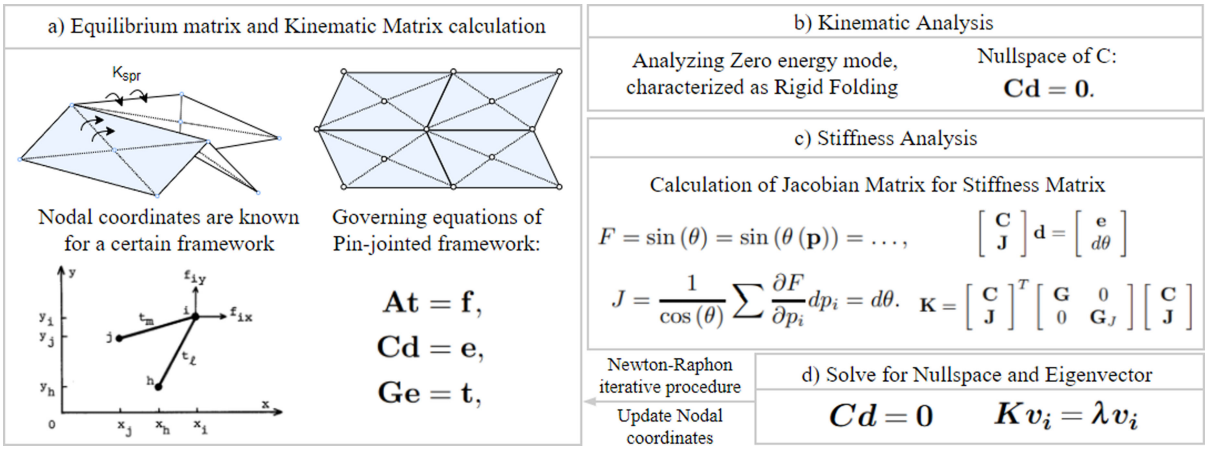

Figure 3. Diagram of the bar and hinge model

of the compatibility matrix (the same as the left nullspace of the equilibrium matrix) indicates a special moving mode called zero-energy mode. In this mode, the joints of the framework will follow a set of nodal displacements without bar elongation, i.e., no bar tension. Therefore, such a zero-energy mode can also be viewed as the rigid folding mode in the field of origami. For a certain framework, nodal coordinates and connection information are known to calculate the equilibrium matrix and compatibility matrix ($C = A^T$), followed by calculating the nullspace of C to obtain a set of nodal displacements representing the zero-energy mode. Alternatively, the stiffness matrix can also be used to obtain the zero-energy mode. Generally, when calculating the stiffness matrix, rotational stiffness around hinges should be considered as well as panel bending, given by

$$\mathbf{K} = \begin{bmatrix} \mathbf{C} \\ \mathbf{J} \end{bmatrix}^T \begin{bmatrix} \mathbf{G} & \mathbf{0} \\ \mathbf{0} & \mathbf{G}_J \end{bmatrix} \begin{bmatrix} \mathbf{C} \\ \mathbf{J} \end{bmatrix}, \tag{2}$$

where **J** is the Jacobian matrix that connects nodal displacement **(d)** and fold angle **(*θ*)**, **G** is the abovementioned diagonal matrix and $\mathbf{G_J}$ indicates the relative importance of the constraint (Schenk and Guest, 2011). However, if the rotational stiffness around hinges is assumed to be much lower than panels or in the kinematic analysis, rigid body assumption is applicable to panels, **G** and $\mathbf{G_J}$ can be reduced to identical matrix **I** and **0** respectively. Then Eq.2 can be rephrased to $\mathbf{K} = \mathbf{C}^{TC}$, followed by the calculation of eigenvalues and corresponding eigenvectors (eigenmodes). Each eigenmode represents a structural deformation mode of the system while the corresponding eigenvalue represents an excitation frequency, which is proportional to the total energy of the system (Filipov et al., 2015). In the kinematic analysis, deformation following zero-energy modes will not introduce additional energy into the system, therefore, the calculated eigenvectors with small eigenvalues can represent zero-energy modes. Consequently, Newton-Raphson iterations methods is used to iteratively update the nodal coordinates by adding increments of selected eigenvectors or nullspaces (i.e. times a nullspace of **C** or an eigenvector of **K** with a sufficiently small value, to limit the deformation to the linear range) to perform the kinematic folding.

2.3. Locomotion mechanism of WOB crawler

With the kinematic model of WOB, the deformation and unfolding/folding behaviors can be comprehensively described, providing essential support for designing the WOB crawler. The locomotion mechanism relies on activating localized movement of a pair of neighboring WOB feet with the other feet fixed. This configuration induces sub-symmetrical global unfolding and folding, resulting in the offcenter movement of the vertex in Plane H shown in Fig.2(A), where Plane H is the sub-symmetrical plane. Friction between the vertex and the ground enables the force generated during folding to be transferred to the ground, facilitating the crawling motion.

Specifically, the direction-sensitive anisotropic friction between the vertex and the ground (f_1 and f_2 towards left and right respectively), as well as the friction between the front foot and the ground (f_3 and f_4 towards left and right respectively, where $f_3 = f_4$), varies during the unfolding and folding process. Reverse movement is facilitated by the local bistability of theWOB mechanism. In Position 1, the valley configuration of the front fold enables the vertex to make contact with the ground. Transitioning the front

fold to a mountain configuration (Position 2) inverts the outer end of the mountain fold, allowing a new vertex to establish ground contact. The anisotropic friction assigned to each vertex is directionsensitive and opposite, enabling a vertex to alternate between functioning as a slider and an anchor point during the folding and unfolding cycle. Ideally, the stride length corresponds to the displacement of the off-center vertex achieved in a complete cycle of folding and unfolding.

2.4. Fabrication and assembly of the WOB Crawler

The WOB crawler comprises an actuator module and a control module. The actuator module includes the WOB and a plate with tracks. The WOB is fabricated using a Fused Deposition Modeling (FDM) 3D printer (QIDI TECHNOLOGY, I-Fast) after being modeled in SolidWorks with four distinct layers (Fig.4(A)). Then it is 3D-printed as a whole piece using two materials: Polylactic Acid (PLA) and Thermoplastic Polyurethane (TPU). The PLA layer provides the in-plane stiffness to panels while TPU layers ensure hinge elasticity. The longest and shortest sides of the panel, *OA* and *OB*, measure 70mm and 35mm, with a total thickness of each panel of 1.5mm.

Mechanical constraints are introduced through the plate with hollow tracks (Fig.4(B)), which restricts the Z-axis movement of four external feet while allowing their motion along the 45° track. This configuration facilitates controlled movement of neighboring points (e.g., A_1 and A_7 in Fig.2(A), called activated feet), enabling the off-center vertex movement along the projected line of Plane H. Additionally, a stabilizing block is mounted at the front of the plate to enhance crawler stability as the front foot (Fig.4(E)), with magnetic plates used to adjust the weight and center of mass. Two M3 screws with sharp ends are used to provide the anisotropic friction, different tilting angles will lead to different anisotropic friction (Fig.4(F) and (G)). One screw is attached to the vertex ofWOB with the bottom acting as vertex 1 (Fig.4(C)) while another screw is attached to the bistable front fold with the bottom acting as vertex 2 (Fig.4(D)).

The control module consists of a 12V power source, a controller (Arduino UNO R3), a DC gear motor, and an L298N Motor Driver Module to manage the motor's rotation direction. The motor is connected to one of the WOB's activated feet to drive the crawler's motion.

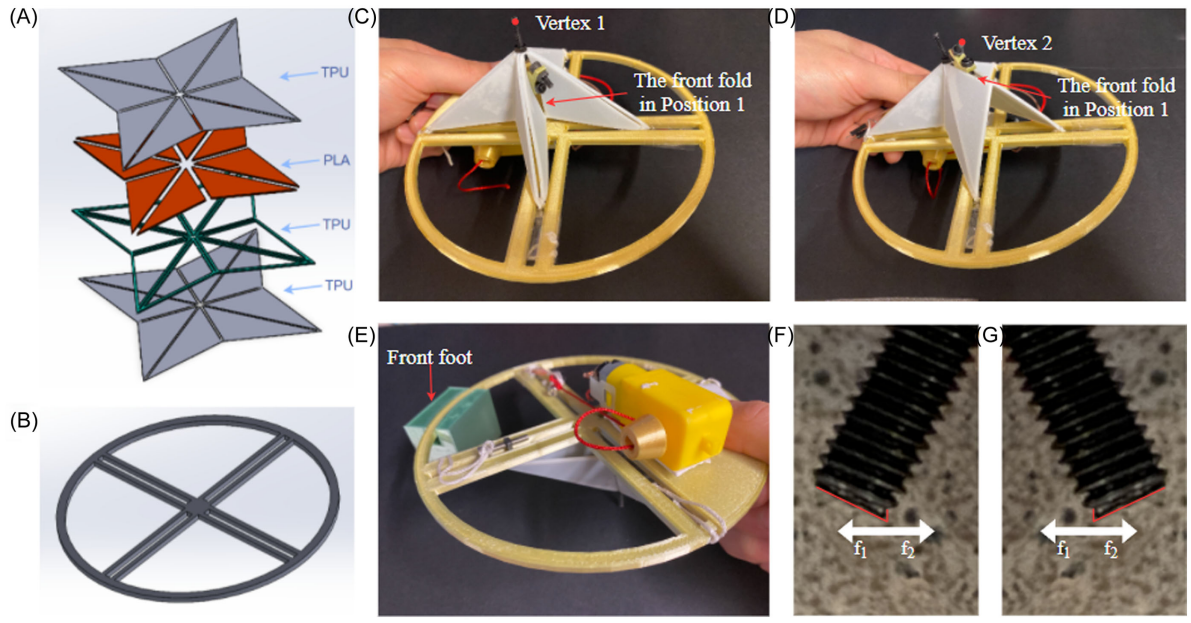

Figure 4. Fabrication and assembly of the WOB Crawler. A) Exploded view of four distinct layers that comprise the WOB. B) Plate with hollow tracks. C) The bottom view of the WOB crawler in Position 1 with the vertex 1. D) The bottom view of the WOB crawler in Position 2 with the vertex 2. E) The top view of the WOB crawler. F) G) M3 screws with a sharp end as the Vertex 1 and 2, of which different tilting angles enable opposite anisotropic friction

3. Result and Discussion

3.1. Kinematic analysis results

The bar and hinge model was applied to analyze the kinematic process of unfolding and folding of the WOB under fully symmetric and sub-symmetric situations. After the kinematic analysis, the nodal coordinates of each node were determined for each iteration, which enables further exploration of the relationships between input variables (such as the displacement of an activated foot) and other dependent parameters.

Under the fully symmetric condition, only one-quarter of WOB was modeled and analyzed. During the folding process, four external feet moved symmetrically toward the center until the valley folds converged at a single line (Fig.5(A)). The relationship between the displacement of the external foot and the mountain fold angle, θ_m is shown in Fig.6(A).

The sub-symmetric analysis examined the folding process between two equilibrium states: the front fold (Bar 1) in the valley configuration (Position 1, Fig.5(B)) and the mountain configuration (Position 2, Fig.5(C)). In this scenario, two neighboring external feet were fixed, while the other two (Nodes 3 and 7) were constrained to move along the 45° track, and the off-center vertex movement was captured. Notably, the local bistability of the structure exhibited a minimal effect on the overall system, as evidenced by the identical vertex trajectories (Fig. 6(B)) and dihedral angle changes between the front two panels (Fig. 6(C)) in both positions.

Additionally, the trajectories of the vertex and the outer end of the front mountain fold (Node 1) were extracted and shown in Fig.6(D), where the Z-coordinates of the vertex and Node 1 in Position 2 were observed to remain at the same level. However, as shown in Fig.6(D), the Z coordinate of Node 1 in Position 1 initially decreased below zero at the start of the folding process before increasing above zero after 5810 iterations, corresponding to a 16.44 mm displacement of Node 3 along the track. This initial decrease represents interference between Node 1 and the plate. To ensure smooth folding and unfolding, the folding process was initiated at the 5,810th iteration (23.48% of the full folding cycle), which will consequently sacrifice the stride length to avoid interference. In contrast, such interference did not occur in Position 2, where the Z-coordinate of Node 1 consistently remained above zero throughout the folding process.

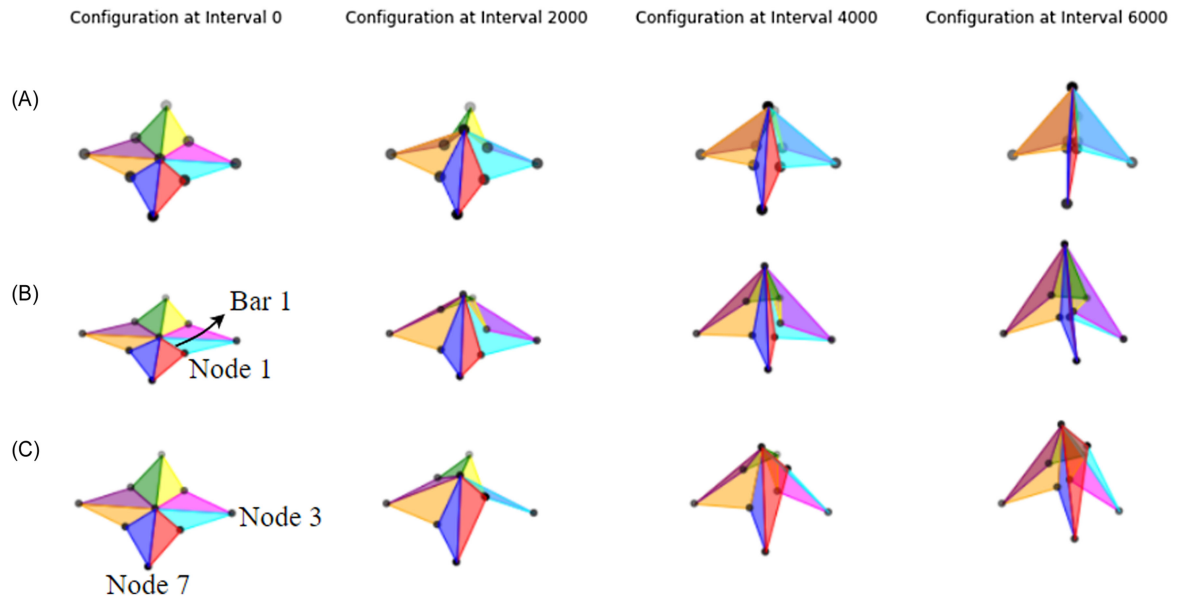

Figure 5. Kinematic analysis results of the WOB. A) Fully symmetric folding process. B) Sub-symmetric folding process in Position 1. C) Sub-symmetric folding process in Position 2

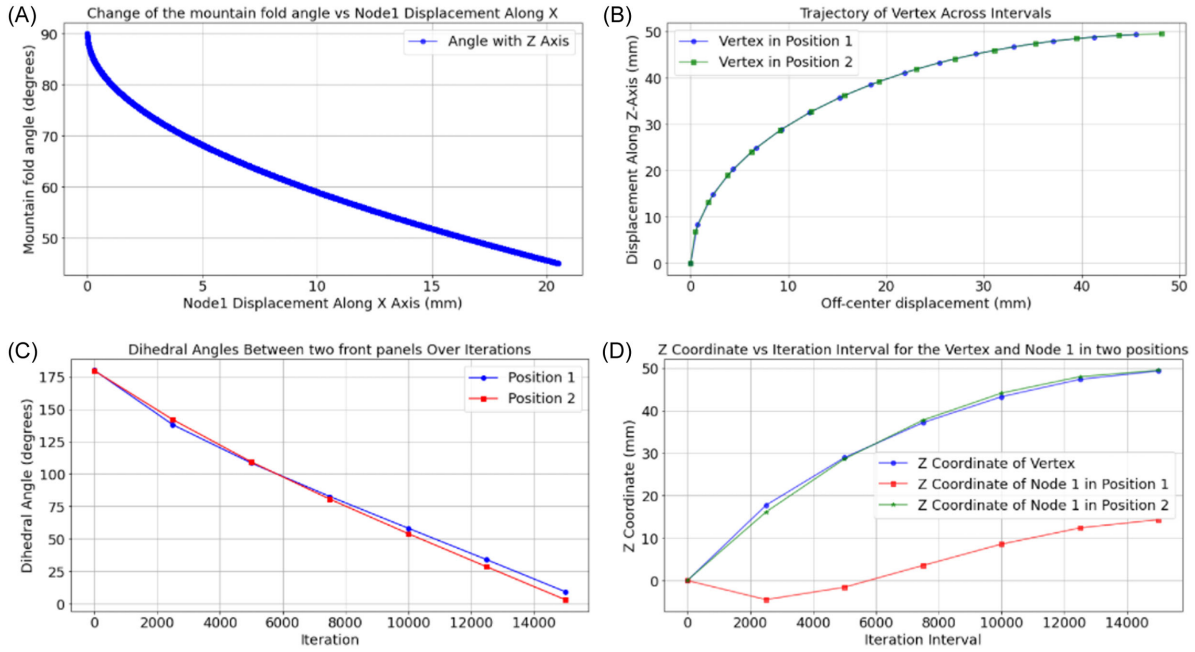

Figure 6. Interested variables of the WOB in fully symmetric and Sub-symmetric folding process. A) The relationship between the mountain fold angle and the Node 1 displacement along the X axis under the fully symmetric situation. B) The trajectory of the vertex in two Positions. C) Dihedral angle between the two front panels in two Positions. D) Z coordinate of Vertex and Node 1 in two Positions

3.2. Experiment Setup

To analyze the performance of the WOB crawler, it was placed on a flat table and actuated for several cycles over a 30-second duration. Each cycle required 1,200 ms for the folding step with about 70 mm of the tendon wound around the motor shaft. The DC gear motor used in this study operated at a nominal speed of 200 rpm (no-load speed) at 6V. The folding ratio, or contraction ratio, ranged from 23.48% to nearly 100%. During the unfolding phase, the elasticity of the fold facilitated a rapid unfolding of the WOB when the motor rotated in reverse. Consequently, the duration of the unfolding step was primarily constrained by the motor's reverse rotation speed.

3.3. Experiment results

The experimental results demonstrate the bi-directional locomotion of the WOB crawler based on its front fold (i.e. Bar 1 shown in Fig.5(B)) configuration. When the front fold is in Position 1, the crawler moves to the left. As shown in Fig.7A, during the folding step, the vertex shifts to the right relative to the plate. This occurs because the friction between the vertex and the ground (f_2) exceeds the friction between the front foot and the ground (f_3 and f_4, where $f_3 = f_4$). Then the vertex functions as an anchor point, enabling the main body of the crawler to move leftward. During the unfolding step (Fig.7B), the higher friction at the front foot $f_4 > f_1$ causes it to serve as the anchor to hold the main body of the crawler at the current location while the vertex retracts to its initial location.

When the front fold transitions to Position 2, the new vertex attached to the front fold will contact with the ground (Fig.7C). During the folding step, the new vertex slides to the right relative to the ground and the main body, as $f_2 < f_3$ and the front foot will perform as the anchor point. While in the unfolding step, higher friction at the vertex ($f_1 > f_4$) secures it to the ground, causing the main body to move rightward. In summary, the direction of motion is dictated by the relative frictional forces. When $f_2 > f_3 = f_4 > f_1$, the crawler moves left, while $f_2 < f_3 = f_4 < f_1$, the crawler moves right. These findings validate the crawler's ability to achieve bidirectional movement by leveraging anisotropic friction and controlled fold configurations.

The WOB crawler was tested to validate its capability for bidirectional movement. In Position 1, the WOB crawler was activated for 30 seconds. Observations from Video 1 revealed relative sliding between

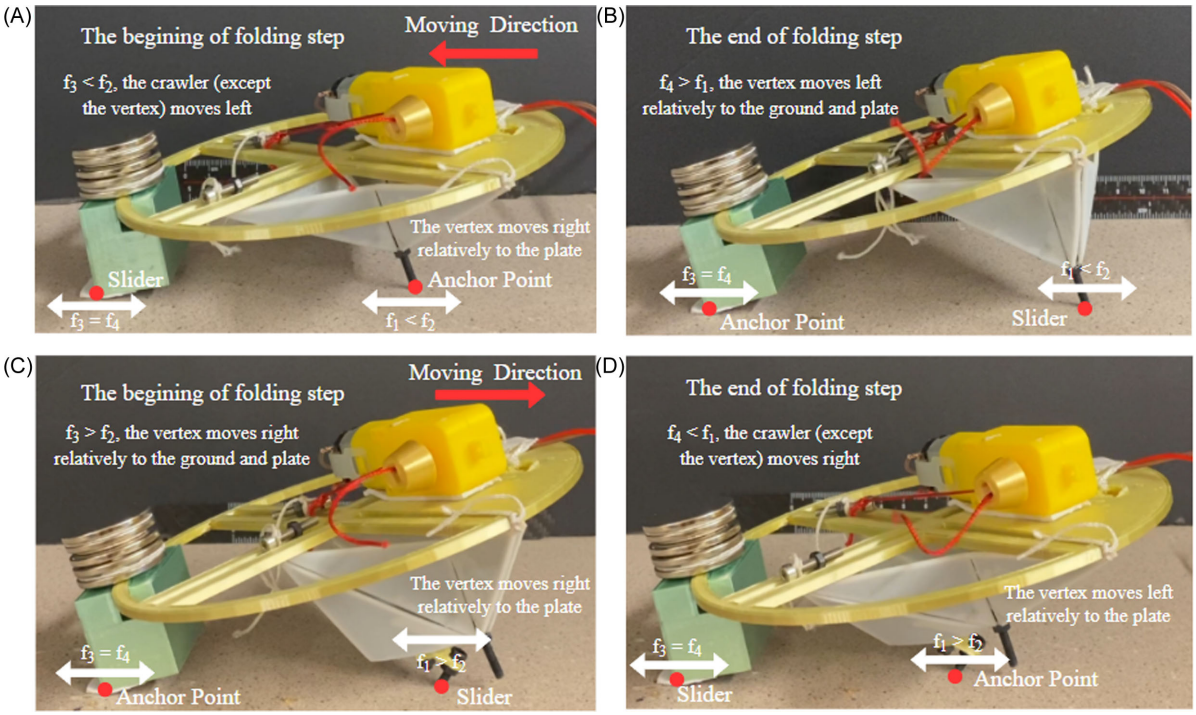

Figure 7. The diagram of folding and unfolding process of the WOB crawler in Position 1 A)B) and Position 2 C)D)

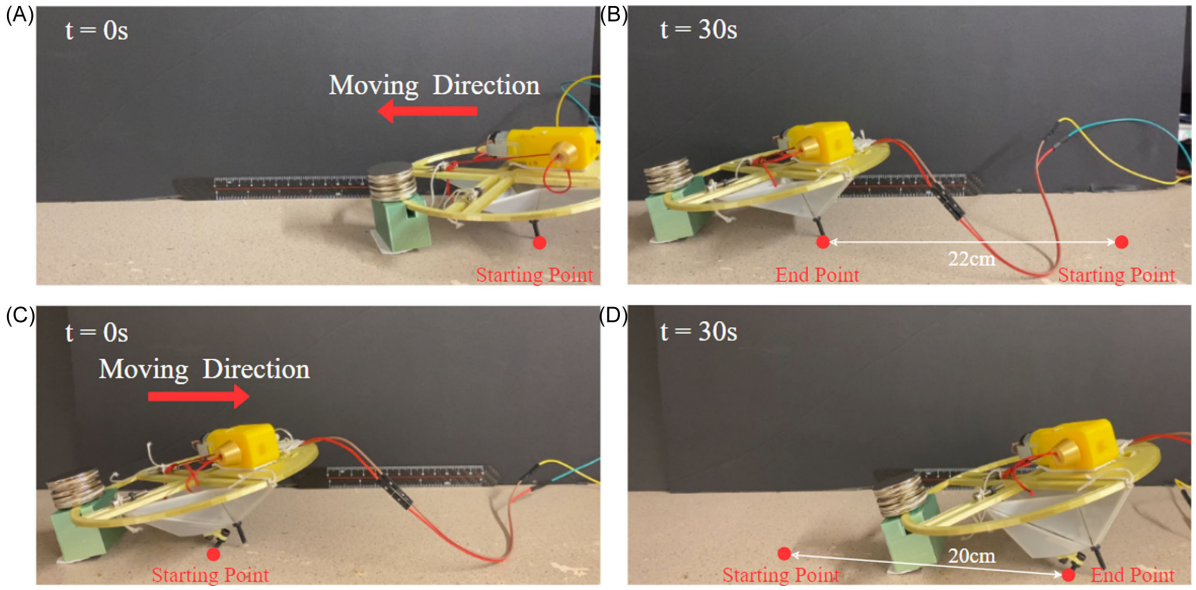

Figure 8. Demonstration of bidirectional movement of the WOB crawler in Position 1 A)B) and Position 2 C)D) within 30 seconds

the vertex (serving as the anchor point) and the ground during the fifth cycle, which impacted the movement efficiency. After 30 seconds, the total displacement of the crawler towards the left was approximately 22 cm (Fig.8(A)(B)). When the bistability of the front fold was manually activated, a new vertex made contact with the ground, and the crawler was again operated for 30 seconds in Position 2. As shown in Video 2, no significant relative sliding between the anchor point and the ground was observed. Without altering the actuation mechanism, the crawler successfully reversed its direction of motion, in agreement with the theoretical analysis presented in Sec. 2.3. However, the total displacement in Position 2 was slightly shorter, measuring approximately 20 cm, attributed to the shorter stride in Position 2 (Fig.8(C)(D)). Further analysis revealed that the front two panels in Position 2 experienced increased

strain, generating higher forces on the front two activated feet and consequently higher friction between the feet and the track. The larger friction caused a reduction in the rotation speed of the motor, thereby decreasing the displacement of the activated foot and reducing the contraction ratio during the folding step.

4. Conclusion

This study presented the development and analysis of a reconfigurable crawler leveraging the principles of waterbomb origami. Inspired by natural adaptability and advanced engineering, the crawler demonstrates innovative capabilities for motion and reconfiguration. The kinematic analysis successfully captures the bistability and deformation mechanics of the waterbomb origami structure, and the results are used to guide the design. By integrating anisotropic friction mechanisms, the crawler achieved bidirectional movement without altering actuation and highlights the potential of origami-inspired designs in advancing multifunctional robotics.

The experimental results validated the theoretical models and demonstrated efficient locomotion and versatility in different configurations. Limitations in stride length and potential interference were identified, suggesting areas for future optimization. Notably, the reconfiguration process currently relies on manual activation, underscoring the importance of future work to develop automated solutions. Future research will also explore the integration of more sophisticated control systems, materials with enhanced durability, and the scalability of the design to broader contexts. The findings underscore the potential of reconfiguration for adaptive and dynamic system designs. While the crawler showcases promising functionality, this design is still at an early stage, and further development is required to transition toward industrial applications.

References

Haupt, R. L. and Lanagan, M. Reconfigurable antennas. *IEEE Antennas and Propagation Magazine*, 55(1):49–61, 2013.

Mintchev, S. and Floreano, D. Adaptive morphology: A design principle for multimodal and multifunctional robots. *IEEE Robotics & Automation Magazine*, 23(3):42–54, 2016.

Lock, R. J., Burgess, S. C. and Vaidyanathan, R. Multi-modal locomotion: from animal to application. *Bioinspiration & biomimetics*, 9(1):011001, 2013.

Baines, R. L., Booth, J.W., Fish, F. E. and Kramer-Bottiglio, R. Toward a bio-inspired variable-stiffness morphing limb for amphibious robot locomotion. *In 2019 2nd IEEE International Conference on Soft Robotics (RoboSoft)*, pages 704–710. IEEE, 2019.

Li, D., Zhao, S., Da Ronch, A., Xiang, J., Drofelnik, J., Li, Y., ... and De Breuker, R. A review of modelling and analysis of morphing wings. *Progress in Aerospace Sciences*, 100:46–62, 2018.

Hassan, M. R., Scarpa, F., Ruzzene, M., and Mohammed, N. A. Smart shape memory alloy chiral honeycomb. *Materials Science and Engineering: A*, 481:654–657, 2008.

Wu, S., Eichenberger, J., Dai, J., Chang, Y., Ghalichechian, N., and Zhao, R. R. Magnetically actuated reconfigurable metamaterials as conformal electromagnetic filters. *Advanced Intelligent Systems*, 4(9):2200106, 2022.

Bordiga, G., Medina, E., Jafarzadeh, S., Bosch, C., Adams, R. P., Tournat, V., and Bertoldi, K. Automated discovery of reprogrammable nonlinear dynamic metamaterials. *Nature Materials*, pages 1–9, 2024.

Patel, D. K., Huang, X., Luo, Y., Mungekar, M., Jawed, M. K., Yao, L., and Majidi, C. Highly dynamic bistable soft actuator for reconfigurable multimodal soft robots. *Advanced Materials Technologies*, 8(2):2201259, 2023.

Chen, Z., Tighe, B., and Zhao, J. Origami-inspired modules enable a reconfigurable robot with programmable shapes and motions. *IEEE/ASME Transactions on Mechatronics*, 27(4):2016–2025, 2022.

Gu, H., Möckli, M., Ehmke, C., Kim, M., Wieland, M., Moser, S., Bechinger, C., Boehler, Q., and Nelson, B. J. Self-folding soft-robotic chains with reconfigurable shapes and functionalities. *Nature Communications*, 14(1):1263, 2023.

Kuribayashi, K., Tsuchiya, K., You, Z., Tomus, D., Umemoto, M., Ito, T., and Sasaki, M. Self-deployable origami stent grafts as a biomedical application of ni-rich tini shape memory alloy foil. *Materials Science and Engineering: A*, 419(1-2):131–137, 2006.

Mao, G., Schiller, D., Danninger, D., Hailegnaw, B., Hartmann, F., Stockinger, T., Drack, M., Arnold, N., and Kaltenbrunner, M. Ultrafast small-scale soft electromagnetic robots. *Nature Communications*, 13(1):4456, 2022.

Tang, Y., Chi, Y., Sun, J., Huang, T.-H., Maghsoudi, O. H., Spence, A., Zhao, J., Su, H., and Yin, J. Leveraging elastic instabilities for amplified performance: Spine-inspired high-speed and high-force soft robots. *Science Advances*, 6(19):eaaz6912, 2020.

Wang, D., Zhao, B., Li, X., Dong, L., Zhang, M., Zou, J., and Gu, G. Dexterous electrical-driven soft robots with reconfigurable chiral-lattice foot design. *Nature Communications*, 14(1):5067, 2023.

Wang, X., Li, S., Chang, J.-C., Liu, J., Axinte, D., and Dong, X. Multimodal locomotion ultra-thin soft robots for exploration of narrow spaces. *Nature Communications*, 15(1):6296, 2024.

Ze, Q., Wu, S., Nishikawa, J., Dai, J., Sun, Y., Leanza, S., Zemelka, C., Novelino, L. S., Paulino, G. H., and Zhao, R. R. Soft robotic origami crawler. *Science Advances*, 8(13):eabm7834, 2022.

Pagano, A., Yan, T., Chien, B., Wissa, A., and Tawfick, S. A crawling robot driven by multi-stable origami. *Smart Materials and Structures*, 26(9):094007, 2017.

Ze, Q.,Wu, S., Dai, J., Leanza, S., Ikeda, G., Yang, P. C., Iaccarino, G., and Zhao, R. R. Spinning-enabled wireless amphibious origami millirobot. *Nature Communications*, 13(1):3118, 2022.

Zhou, H., Grasinger, M., Buskohl, P., and Bhattacharya, K. Low energy fold paths in multistable origami structures. *International Journal of Solids and Structures*, 265:112125, 2023.

Zhu, Y., Schenk, M., and Filipov, E. T. A review on origami simulations: From kinematics, to mechanics, toward multiphysics. *Applied Mechanics Reviews*, 74(3):030801, 2022.

Pellegrino, S. and Calladine, C. R. Matrix analysis of statically and kinematically indeterminate frameworks. *International Journal of Solids and Structures*, 22(4):409–428, 1986.

Filipov, E. T., Liu, K., Tachi, T., Schenk, M., and Paulino, G. H. Bar and hinge models for scalable analysis of origami. *International Journal of Solids and Structures*, 124:26–45, 2017.

Schenk, M. and Guest, S. D. Origami folding: A structural engineering approach. *Origami*, 5:291–304, 2011.

Filipov, E. T., Tachi, T., and Paulino, G. H. Origami tubes assembled into stiff, yet reconfigurable structures and metamaterials. *Proceedings of the National Academy of Sciences*, 112(40):12321–12326, 2015.